CHAPTER III

METHODOLOGY

3.1 Introduction

Over more than two decades of widespread application, receiver function technique has emerged as an effective means for structural analysis of the earth by mapping seismic discontinuities in the crust and upper mantle.

A seismic discontinuity is defined to be the boundary between two layers of strong detectable contrast in seismic impedance. Fig. 3.1 is a schematic representation of global seismic discontinuities in a one dimensional stratified earth (according to IASP91 velocity model, *Kennett & Engdahl 1991*). Of main interest In this study are the Moho (the crust−mantle boundary) and two major upper mantle discontinuities at 410 km and 660 km depths which are globally observed.
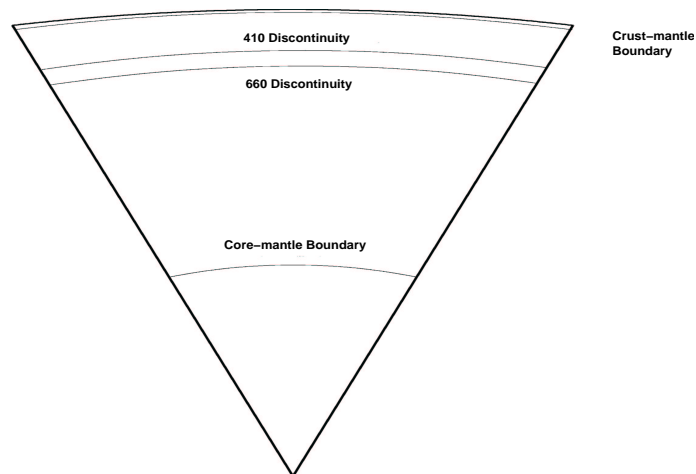

Fig. 3.1 Schematic cross section of the Earth, showing major seismic discontinuities; the crust−mantle boundary, 410km and 660km upper mantle discontinuities and core−mantle boundary (according to IASP91 global velocity model).
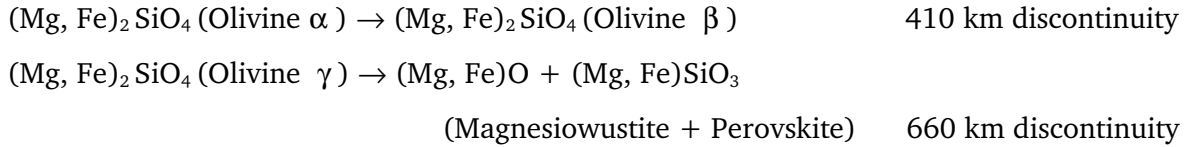
3.1.1 The Moho

The Moho is a boundary of highly variable seismic character that separates the crust from the upper mantle. It was first discovered in 1910 by Mohorovicic who noticed an abrupt increase in seismic wave velocities under an area with thin crust in Europe. It is believed that the seismic contrast between the crust and the upper mantle is of chemical nature. P wave velocity in Feldspar which is the most abundant constituent mineral in the crust is about 6.0 km/sec while Olivine which signifies the main component of the upper mantle has a P wave velocity of 8.5 km/sec according to laboratory measurements. However, the Moho is not always a first order discontinuity and could behave as a transitional compositional gradient which makes it seismically undetectable.

3.1.2 Upper mantle and the 410 and 660 discontinuities

The upper mantle just below the crust is a region of high seismic velocities ($8-8.5$ km/sec) which is known as lid. The lid overlies a low velocity zone (LVZ or asthenosphere) which was first discovered by Gutenberg in 1959. The boundary between lithosphere and asthenosphere is not seismically detectable on a global scale. The 410 km and 660 km discontinuities are on the other hand globally observed and define the upper mantle transition zone.

The discovery of the upper mantle discontinuities dates back to 1936 as Jeffreys noticed and interpreted some kinks in travel time curves as strong velocity contrast across discontinuities in upper mantle. Unlike the crust$-$mantle boundary which is of compositional nature it is widely accepted that mineralogical phase transformations are responsible for abrupt velocity increases across 410 and 660 discontinuities. The high temperature high pressure laboratory experiments show that the following phase changes could be considered as likely and plausible cause of ample seismic observations:

(Mg, Fe)$_2$ SiO$_4$ (Olivine α) $\rightarrow$ (Mg, Fe)$_2$ SiO$_4$ (Olivine β)   410 km discontinuity

(Mg, Fe)$_2$ SiO$_4$ (Olivine γ) $\rightarrow$ (Mg, Fe)O + (Mg, Fe)SiO$_3$

$\qquad\qquad\qquad\qquad$ (Magnesiowustite + Perovskite)   660 km discontinuity

Given the visibility of the 410 and 660 transition zones to short period seismic waves (periods up to 1 sec, e.g. *Benz & Vidale 1993*) they can only arise from thin gradient zones not thicker than 4−5 km to meet the quarter (or less) of a wavelength requirement (*Richards 1972*). Early experimental results demanded too broad a zone to produce observed seismic characteristics, an obstacle that was removed by improved thermodynamic constraints (e.g. *Bina & Wood 1987*).

3.1.3 Discontinuities and their fingerprints on the P coda

As seismic rays cross discontinuities, the energy of the incoming ray is partitioned between reflected and refracted rays. In a special case when a P wave impinges on a boundary four derivative waves, refracted P, refracted SV, reflected P, reflected SV are resulted that are as shown in Fig. 3.2.
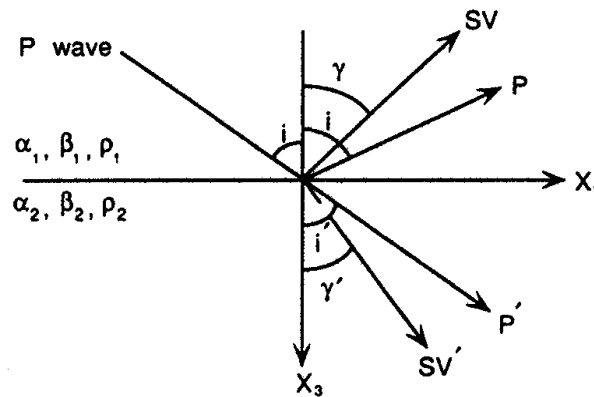

Fig. 3.2 The ray geometry for an incident P wave on a solid−solid interface and the resulting four derivatives; refracted P (**P'**), reflected P (**P**), refracted SV (**SV'**), reflected SV (**SV**). α, β and ρ represent P wave velocity, S wave velocity and density, respectively.

The geometry of the incident P wave and its derivatives (Fig. 3.2) is governed by Snell's law,

$$(\text{Sin } i\,)/\alpha_1 = (\text{Sin}\gamma)/\beta_1 = (\text{Sin}\gamma\,')/\beta = (\text{Sin } i\,')/\alpha_2 \quad (3.1)$$

whereas the amplitudes of the partitioned energy are determined by wave−field theory and represented by reflection and transmission coefficients.

Receiver function method is a way to detect, isolate and enhance P−to−SV conversion mode which is produced as teleseismic P waves cross a seismic discontinuity. For a planar P wave incident on a solid−solid interface the transmission coefficient of P−to−SV (Eq. 3.2) can be deduced from D' Alembert's solution (*Lay & Wallace 1995*). Even with the plane wave assumption the equation has a complicated form:

$$\mathbf{T_{PS}} = [\mathbf{2}\rho_1\,\eta_{\alpha 1}\,\boldsymbol{Hp}(\alpha_1\,/\beta_1)]\,/\,\mathbf{D} \qquad (3.2)$$

Where (ρ, the density, α and β, P and S wave velocities, respectively and p and η, horizontal and vertical slownesses, respectively),

$a = \rho_2(1{-}2\beta_2^{\,2}\,p^2) - \rho(1{-}2\beta_1^{\,2}p^2)$ $\qquad\qquad$ $E = b\eta_{\alpha 1} + c\eta_{\alpha 2}$ $\quad (3.3)$

$b = \rho_2(1{-}2\beta_2^{\,2}p^2) - 2\rho_1\beta_1^{\,2}p^2$ $\qquad\qquad$ $F = b\eta_{\beta 1} + c\eta_{\beta 2}$ $\quad (3.4)$

$c = \rho_1(1{-}2\beta_1^{\,2}p^2) - 2\rho_2\beta_2^{\,2}p^2$ $\qquad\qquad$ $G = a - d\eta_{\alpha 1}\eta_{\beta 2}$ $\quad (3.5)$

$d = 2(\rho_2\beta_2^{\,2} - \rho_1\beta_1^{\,2})$ $\qquad\qquad$ $H = a - d\eta_{\alpha 2}\eta_{\beta 1}$ $\quad (3.6)$

$$D = EF + GHp^2 \qquad\qquad (3.7)$$

This complex equation could be better understood by depicting $\mathbf{T_{PS}}$ as a function of three variables, i.e., Vp, Vs, and density (ρ) and comparing the results as all three parameters change simultaneously in Fig. 3.3 (after *Yuan 1999*). It is clearly seen that the Vs contrast (and consequently Vp/Vs) across the discontinuity is the most important parameter affecting the conversion coefficient whereas changes in Vp or density (ρ) have no significant effect.
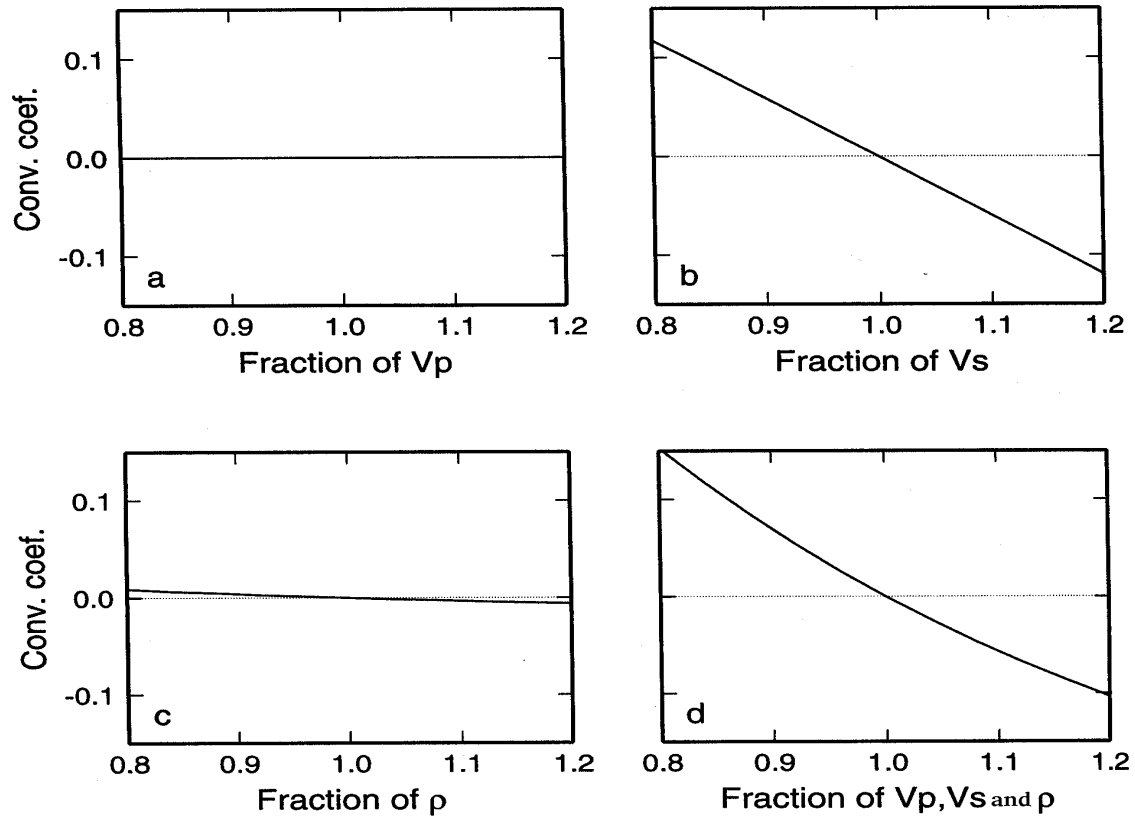
Fig. 3.3 Variation of P−to−SV conversion coefficient (T_{PS}) at a solid−solid interface first against changes of one of the variables; Vp, Vs, and ρ (Figs. 3.3a, 3.3b, and 3.3c, respectively) above the interface and finally as all three parameters change simultaneously (Fig. 3.3d). Below the interface the parameters of the medium is fixed as: Vp=8 km/s, Vs=4.6 km/s, and ρ = 3.3 g/cm³. The parameters above the interface are changed from 80% to 120 % of the values below the interface while Vp/Vs=1.732 is kept constant and ρ is changed according to Birch Law: ρ = 0.32Vp + 0.77. It is shown that the T_{PS} is only sensitive to changes of Vs (after *Yuan 1999*).

Apart from changes in Vs (and consequently Vp/Vs) across the discontinuity the incidence angle of impinging P wave on a boundary has a significant effect on the amplitude of the SV conversions. This has been shown in Fig. 3.4 where variations of the reflection and refraction coefficients as a function of incidence angle of the P wave hitting a boundary from high velocity towards the low velocity medium, are depicted.
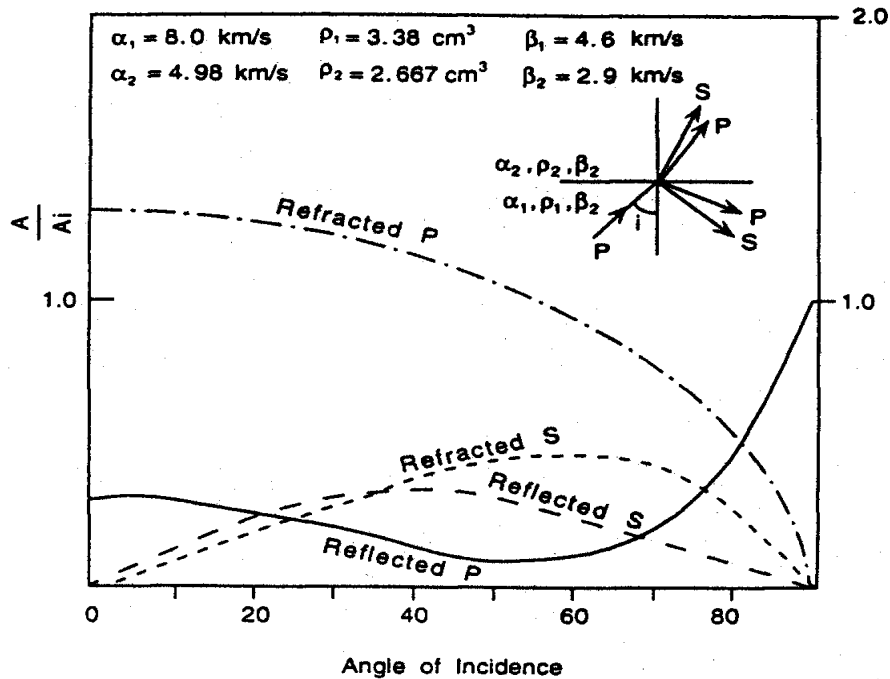

Fig. 3.4 Variations of the reflection and refraction coefficients as a function of the P wave incidence angle on a solid−solid boundary from high velocity medium (after *Lay and Wallace 1995*).

By following the "refracted S" curve in Fig. 3.4, it becomes clear that the transmission coefficient is directly proportional to the incidence angle. In other words the amplitude of P−to−S conversion from a certain discontinuity and for a given earthquake magnitude reduces with increasing epicentral distance.

39

Although the teleseismic P waves of a given earthquake hit the 410 km and 660 km discontinuities with higher incidence angle than they pierce through the Moho, the transmission coefficient at upper mantle discontinuities is about an order of magnitude smaller than at the Moho.

In order to take advantage of planar wave approximation and avoid complications of dealing with interfering PP and upper mantle triplication phases, teleseismic P waves recorded in epicentral distances of larger than 30º are used. The upper bound can theoretically be set at the epicentral distance of 103º (beginning of the P wave shadow zone). Practically though with respect to decreasing amplitudes of conversions with increasing distance (mentioned above) and in the presence of background noise earthquakes with magnitudes of at least 5.7 or higher up to distances of 95º are used for receiver function analysis.

3.2 Receiver function calculation

To isolate, detect and enhance the SV phases hidden in the P coda of teleseismic earthquakes following steps are taken:

3.2.1 Restitution

A seismogram recording could be formulated as:

$$\mathbf{S(t) = A(t) * E(t) * I(t)} \qquad (3.8)$$

where $\mathbf{S(t)}$ is the time domain recorded seismogram, $\mathbf{A(t)}$ far field seismic source function, $\mathbf{E(t)}$ the earth response and $\mathbf{I(t)}$ is the instrument response function.

In order to take the first step towards isolating receiver effects the seismograms must be corrected for the instrument response. Considering the broad response of broadband

seismometers restoring the ground displacement (or velocity) does not change the frequency content of the seismograms significantly. Removing the instrument response of the short period and wide−band seismograms on the other hand can broaden the response of the seismograms.

In the presence of abundant seismic noise deconvolving the instrument response from seismograms might turn out to be unstable by introducing noise amplification. This phenomenon decreases useful frequency band of the corrected signals (Fig. 3.5).
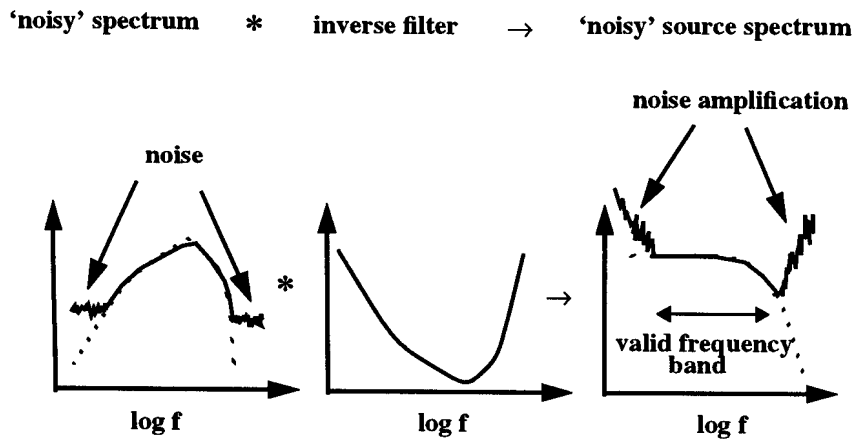
'noisy' spectrum   **∗**   **inverse filter**   →   **'noisy' source spectrum**

Fig. 3.5 Schematic representation of instrument correction by convolving the recorded seismogram with the inverse of the instrument response. It is shown how background noise can increase the noise on the corrected spectrum and thereby the valid frequency band is decreased (after *Scherbaum 1992*).

Since useful teleseismic waves for receiver function studies have frequencies less than 1 Hz lowpassing the seismograms before removing the instrument response can improve signal to noise ratio without losing useful information.

When recordings from different types of seismographs are to be utilized (as might be the case with temporary networks) instrument correction is vital for equalizing the seismograms for various instrument responses.

41

3.2.2 Rotation

Teleseismic P waves in epicentral distances of $30^\circ - 100^\circ$ approach the recording stations with very acute incidence angles. Therefore, with respect to particle motions, SV phases are best recorded on horizontal components (Fig. 3.6).
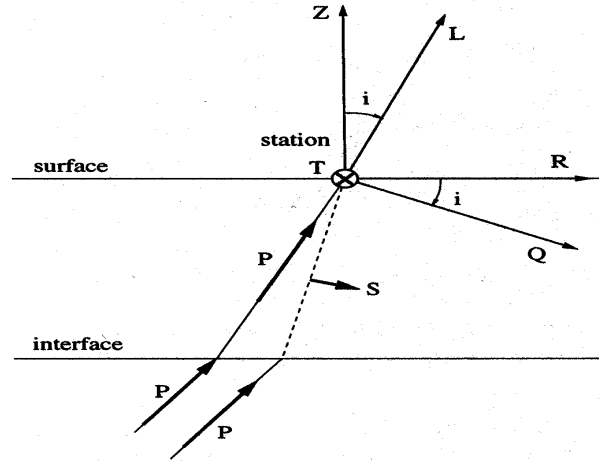

Fig. 3.6 Sketch showing the incident teleseismic P wave on a horizontal boundary from high velocity medium and recorded in a receiving station. The incoming P wave is on $x_1 x_3$ plane and therefore no SH motion is expected. Labels **L**, **Q**, and **T** represent the axes of the ray coordinate system whereas **R** and **T** represent the radial and transverse axes in $2 - $D rotation.

In the conventional $2 - $D rotation scheme (for which only the azimuth of the incoming ray is needed) the horizontal components (**NS**, and **EW**) are rotated into Radial (**R**) and Transverse (**T**) components. Therefore, most of the the desired SV energy is confined to radial component, whereas the vertical (**Z**) component contains most of the P wave energy. A P wave incident on a horizontal boundary owing to its particle motion being confined in $x_1 x_3$ plane produces no SH wave (Fig. 3.6). However, steeply dipping discontinuities, lateral inhomogeneities and anisotropy may contribute to appearance of SH energy on the **T** component.

Projection of the incoming teleseismic P wave in the ray coordinate system of **L**, **Q** and **T** (Fig. 3.6) shows that rotating the recorded components into this 3−D system has the advantage of better confining **P**, **SV** and **SH** energy to **L**, **Q** and **T** components respectively than **Z, R, T** system.

However, a prerequisite for the success of this method of rotation is correct estimation of the incidence angle of arriving P wave. Overestimation or underestimation of the incidence angle can produce unwanted peaks and troughs at the time the direct P wave is expected (Fig. 3.7). Fortunately, these uncertainties only affect the observed delay times of the P−to−S conversions from very shallow (a few kilometers deep) conversions.

The Azimuth and incidence angle of incoming P wave can be either theoretically calculated or actually measured. Knowing the position of the earthquake hypocenter and the coordinates of the recording station it is possible to calculate the Azimuth and incidence angle of incoming P wave using a global velocity model (here IASP91, *Kennett and Engdahl 1991*). In order to account for scattering just beneath the stations it is advisable to measure azimuth and incidence angle by particle motion observation of the first few seconds of P wave after its onset. This could be more effective if the traces are filtered by a low pass 1 Hz filter to rid the signals from unwanted high frequency details.

If the incidence angle and azimuth of the incoming P wave are correctly estimated and the conversion phases do not originate from discontinuities dipping more than 10° (*Langston 1977*) the first goal of isolating the desired SV energy in the P coda is achieved. Moreover, since the first onset on the Q component is the SV phase it is theoretically possible to detect discontinuities even if they are located at shallow depth. This is in contrast to the radial component where the direct P arrival usually masks P−to−SV conversions from very shallow discontinuities.
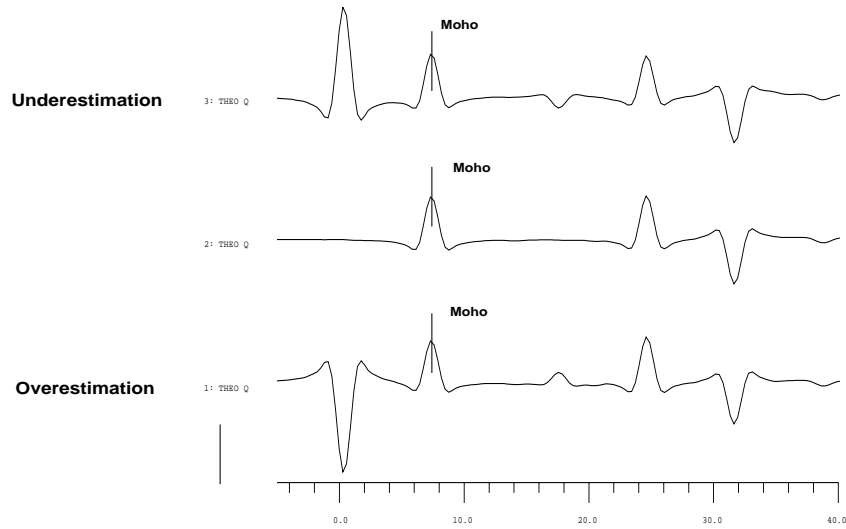
Fig. 3.7 Rotated synthetic receiver functions (**Q**) calculated using reflectivity method (*Kind 1985*) (for a modified IASP91 velocity model with a curstal thickness of 60 km, crustal Vp and Vs values of 6.5 Km/s and 3.75 km/s respectively, epicentral distance of 68°, and the earthquake focal depth of 600 km) resulted from rotation of R and Z components with three incidence angle values. The middle trace shows the result of rotation of the R and Z components for measured incidence angle of 23.52°. The bottom trace is the result of rotation for an assumed incidence angle of 33.52° (overestimation) and the top trace is that of rotation for an incidence angle of 13.52° (underestimation). For both underestimation and overestimation there are spurious signals which might hide signals coming from very shallow sources.

3.2.3 Source and path equalization by deconvolution

Three restituted components after rotation can be theoretically represented by:

$$D_L(t) = S(t) * E_L(t) \qquad (3.9)$$

$$D_Q(t) = S(t) * E_Q(t) \qquad (3.10)$$

$$D_T(t) = S(t) * E_T(t) \qquad (3.11)$$

44

By assuming $E_L(t) \approx \delta(t)$, deconvolution of $D_L(t)$ from $D_Q(t)$ removes the effect of the source and the result is the receiver structure at the recording station:

$$E_Q(\omega) = D_Q(\omega) / D_L(\omega) \qquad (3.12)$$

Where $D_Q(w)$ and $D_L(w)$ are the frequency−domain representation of the recorded **Q** and **L** components of true ground displacements.

In practice due to instability of frequency deconvolution, spiking deconvolution which is done in time domain, has been used in this study. Spiking deconvolution is the process of compressing a seismic wavelet (here **L** component) into a zero−lag spike. The spiking deconvolution operator is strictly the inverse of the initial segment of the **L** component (usually 20−40 seconds following the P onset, which contains most of the P wave energy) and is obtained by minimizing the least square differences between the observed seismogram and the desired delta−like spike function. The process which is called least−squares inverse filtering is a special case of optimum Wiener filter. The acquired inverse filter is then convolved with the **L**, **Q** and **T** components to obtain desired zero−lag spike, source equalized **Q** (called the Receiver Function) and deconvolved **T** components. Finally the deconvolved traces are normalized to the maximum amplitude of the spike on the **L** component. It is obvious that through deconvolution the absolute time of the seismograms is lost and all timing information will be relative to direct **P** arrival which is marked by the spike peak, positioned at zero in the deconvloved **L** component.

Deconvolving the **L** component from the **Q** component has a clear advantage over the alternative method of deconvolving the vertical component from the radial component so that the resulting receiver functions are free from direct **P** arrivals and therefore converted phases originating from shallow discontinuities can be detected more easily (Fig. 3.8).
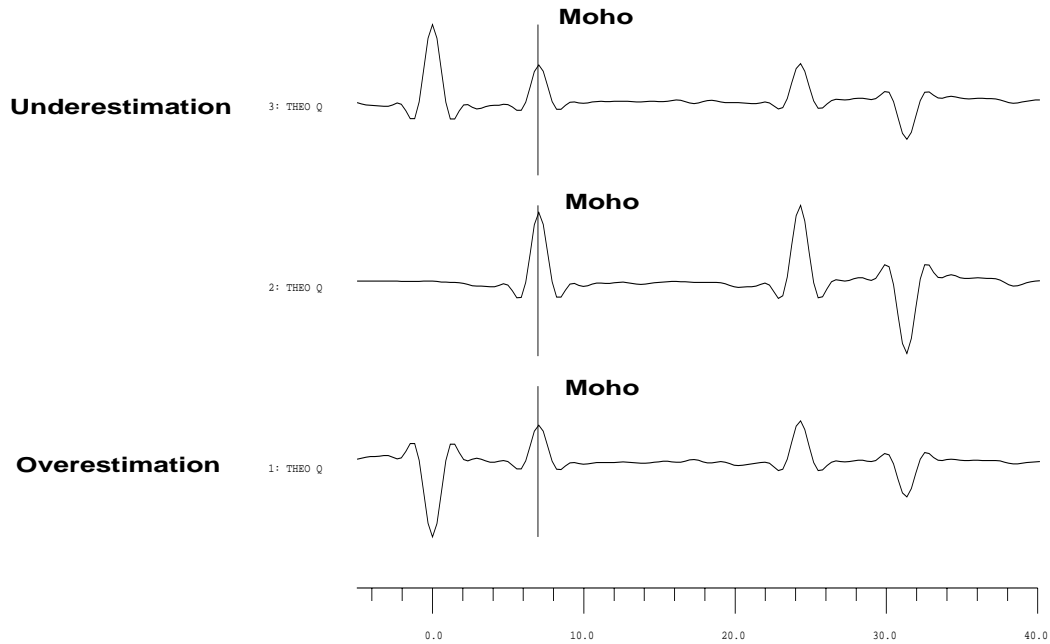
Fig. 3.8 Synthetic receiver functions produced by deconvolving Q components (Fig. 3.7) from their corresponding L components using despiking deconvolution method. The conversion from the Moho (at 60 km depth) is marked.

3.3 Distance equalization by move−out correction

The P−to−S conversion phases are usually of low amplitude and therefore for the purpose of detection and amplification it is necessary to align and stack receiver functions from different epicentral distances at each station. However, successful alignment and constructive summation of conversion phases requires that the receiver functions be equalized in terms of their ray parameters.

For the simple case of a single layer over a half space, Fig. 3.9 shows the geometry of the incident P and the P−to−SV as generated at the interface and recorded in a receiver station. With regard to epicentral distances involved ($\Delta > 30°$) it is acceptable to approximate the

incoming P waves as plane waves and accordingly formulate the The Ps−P delay time as:

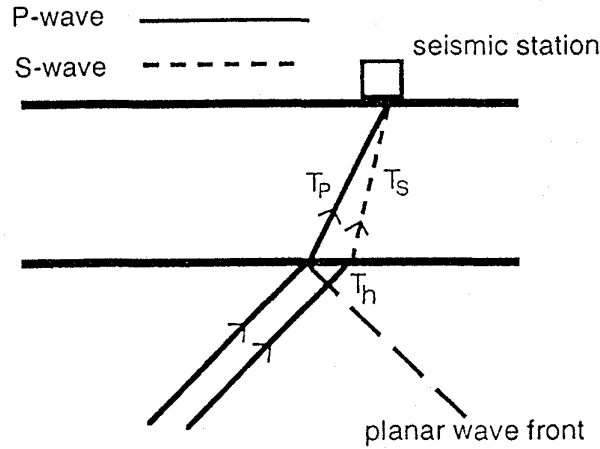$$\Delta T_{Ps} = T_S + T_h - T_P \qquad (3.13)$$

Fig. 3.9 Scheme showing the ray paths of direct P and Ps for a layer over a half space. T_P and T_S are the traveltimes of the P and S phases, respectively and assuming the same ray parameter for both. T_h is the traveltime difference of the two rays in the half space with planar wave approximation.

Assuming that the ray parameters are the same for P and Ps it can be shown (*Kind and Vinnik 1988*) that,

$$\Delta T_{Ps} = h(\ (V_S^{-2} - p^2)^{1/2} - (V_P^{-2} - p^2)^{1/2}) \qquad (3.14)$$

and following the same line of argument the delay times for important crustal reverberations are calculated as follows:

$$\Delta T_{PpPs} = h(\ (V_S^{-2} - p^2)^{1/2} + (V_P^{-2} - p^2)^{1/2}) \qquad (3.15)$$

47

$$\Delta T_{PpSs/PsPs} = 2h(\ V_S^{-2} - p^2\ )^{1/2} \hspace{2cm} (3.16)$$

$$\Delta T_{PsSs} = h(\ 3(V_S^{-2} - p^2\ )^{1/2} + (V_P^{-2} - p^2\ )^{1/2}\ ) \hspace{0.5cm} (3.17)$$

The conversion from crust−mantle boundary, its crustal multiples and the upper mantle 410 km and 660 km discontinuities arrive at the recording station with different slowness values (Fig. 3.10).

An approach, very similar to familiar normal move−out correction in exploration seismology, is taken to adjust the times of Ps conversions of all receiver functions to what would have been recorded at 67° (corresponding to ray parameter= 6.4 sec/°) according to a global one dimensional velocity model (here IASP91 global velocity model). The correction stretches the time scale of receiver functions of larger than 67° while those of the shorter distances are contracted. Consequently all direct conversions from Moho and upper mantle appear as straight lines whereas crustal multiples will appear even more inclined (Fig. 3.11).
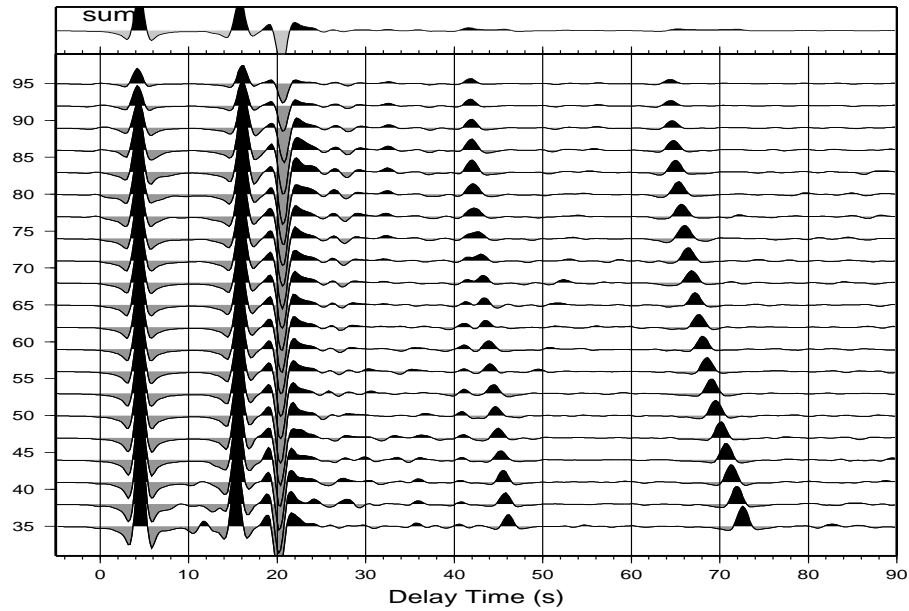
Fig. 3.10 Synthetic receiver functions calculated for a single three component station with reflectivity method (*Kind 1985*) using modified IASP91 model containing a 40 km thick crust. Crustal Vp and Vs have been set to 6.5 Km/s and 3.75 km/s respectively. Epicentral distances range from 35° and 95° with focal depth fixed at 600 km. It is shown that by increasing epicentral distance the delay times of Ps conversions decrease while those of the multiples increase.
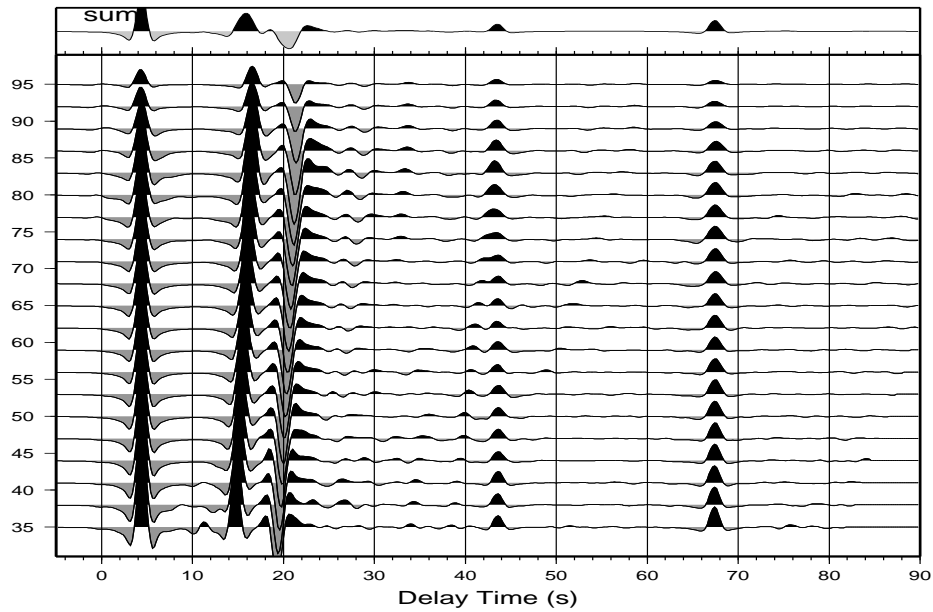

Fig. 3.11 Move−out corrected receiver functions of Fig. 3.10 using IASP91 velocity model and taking the epicentral distance of 67° (slowness of 6.4 sec/°) as reference. While the converted phases from Moho, 410 km and 660 km discontinuities appear straight, the crustal multiples are slant. The summation traces shows the amplification of converted phases whereas the multiples are suppressed.

In the case of upper mantle discontinuities the curvature of the Earth becomes important and unlike Moho conversions has to be taken into account. Since all move−out equations presented above are valid for flat−layered earth an earth flattening approximation subroutine has been used to account for sphericity.

Now aligning the move−out corrected receiver functions according to epicentral distances not only helps to distinguish the direct conversions. It also allows for enhancement of conversions by constructive summation (stacking) of amplitudes direct conversion whereas the multiples will be substantially suppressed (Fig. 3.11).

Move−out correction can also be applied to crustal reverberations. Applying the correction to each multiple and aligning the corrected seismograms by epicentral distance leads to straight appearance of the multiples whereas the direct conversions are inclined. After the correction is applied those reverberations which have similar ray parameters appear parallel to each other made. It is obvious that stacking the seismograms corrected for multiple move−outs enhances multiples while direct conversions are considerably weakened (Fig. 3.12).
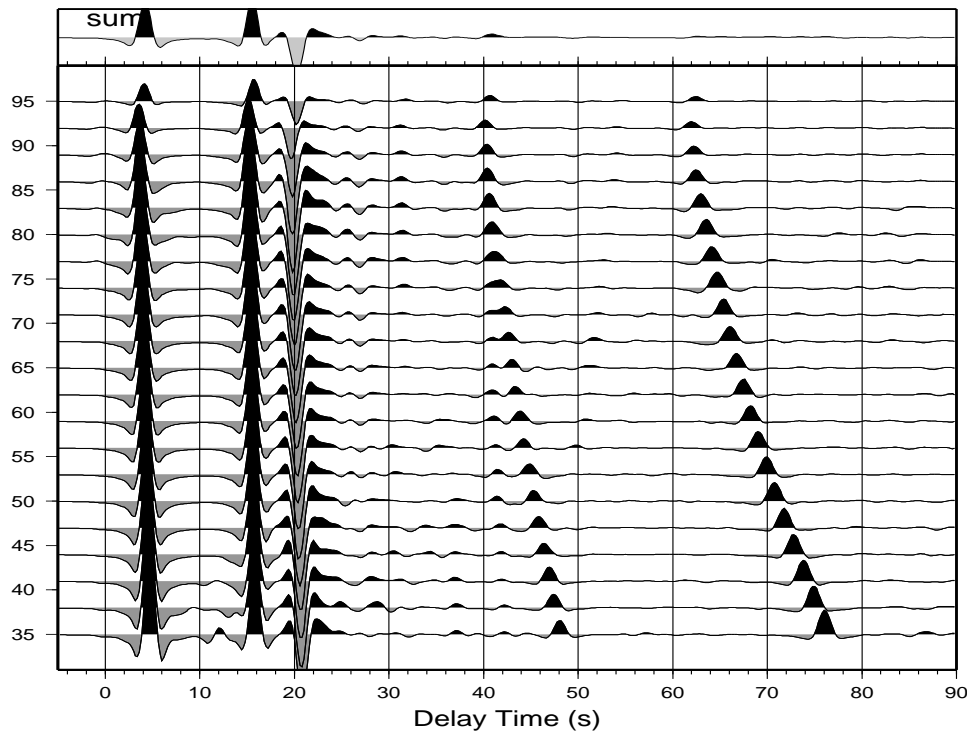
Fig. 3.12 Move−out correction applied to PpPs multiples of the receiver functions in Fig. 3.10. IASP91 velocity model is used and the reference slowness of 6.4 sec/° (Δ = 67°) is chosen. While multiples appear straight the Ps conversions are inclined. This leads to enhancement of the multiples and suppression of the Ps conversions in the summed trace in the top of the panel.

3.4 Receiver function migration

To improve the spatial resolution and translate the delay times into depths, the Ps amplitudes on each receiver function can be back projected along the ray path onto the spatial locations of the conversion points in a process similar to migrating CMP's (in exploration seismology) to their true locations (*Kosarev et al. 1999*) (Fig. 3.13). The ray paths are calculated using a one dimensional global velocity model (here IASP91, *Kennett & Engdahl 1991*) with assumption that conversions originate from planar interfaces. Sometimes a spatial smoothing filter is used to improve the spatial correlation so that the space is gridded and back projected amplitudes originating from adjacent boxes are stacked to improve signal to noise ratio.
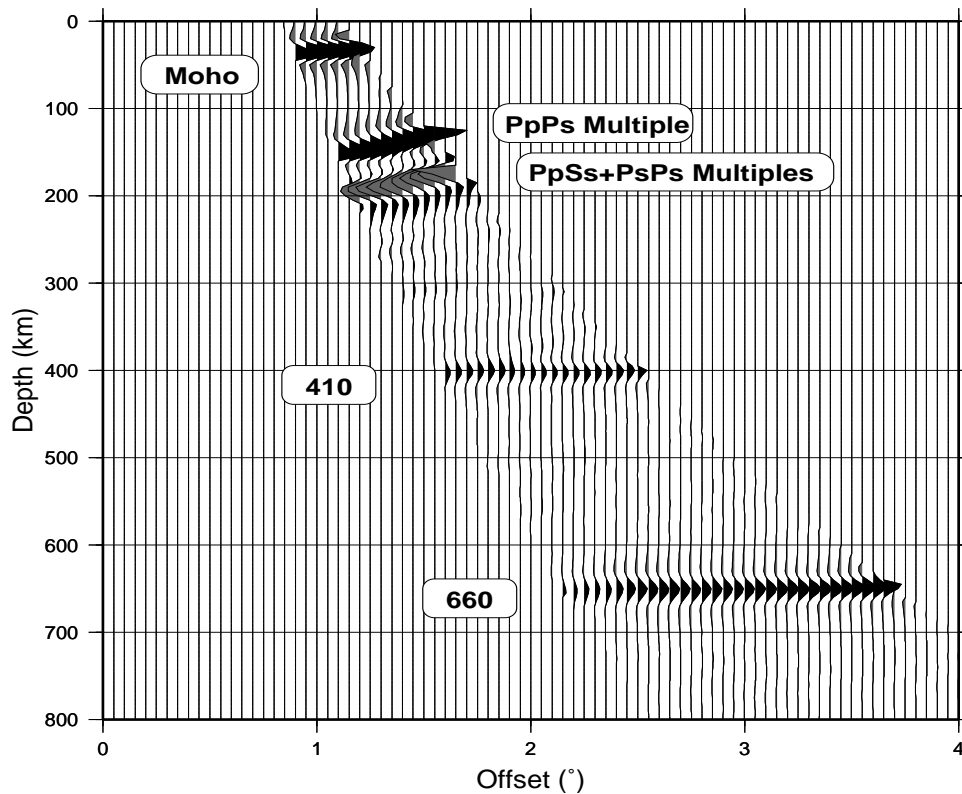

Fig 3.13 Migration of synthetic functions of Fig. 3.10 by tracing the P−to−S amplitudes to their points of conversion. Since all earthquakes approach the station with the same azmiuth the result is 2−D. For ease of identification the phases are labeled. The oblique appearance of crustal multiples helps to distinguish them from direct conversions.

Applying the method to data from station arrays and networks where ray paths from neighboring stations, specially at large depths cross one another improves the signal quality significantly. Besides, projection of 3−D data along desired 2−D sections can further amplify the conversion amplitudes while suppressing the reverberations due to their oblique appearance (Fig. 3.13).

The technique can also be applied to reverberations of conversions and thus provide an additional possibility for detecting direct conversions.

3.5 Estimating the crustal depth and Vp/Vs ratio

Given average crustal velocities the delay times of Moho Ps conversion and its multiples can be used to estimate the crustal thickness (equations 3.14−3.17). However, since the depth to the Moho trades off strongly with the crustal Vp/Vs ratio Zhu & Kanamori (*Zhu & Kanamori 2000*) proposed a stacking algorithm which sums the amplitudes of receiver functions at the predicted arrival times of the Moho conversion phase and its multiples (**Ps**, **PpPs**, and **PpSs+PsPs**) for different crustal thickness h and **Vp/Vs** ratios. Consequently time domain receiver functions are mapped into h vs. **Vp/Vs** domain without the necessity to read phases.

With respect to higher SNR of direct Ps than its multiples, amplitudes of different phases are weighted and stacked according to:

$$s(h, \textbf{Vp/Vs}) = w_1 * Q(t_1) + w_2 * Q(t_2) - w_3 * Q(t_3) \quad (3.18)$$

where $Q(t_i)$ are the receiver function amplitudes, t_1, t_2, and t_3 are the predicted **Ps**, **PpPs**, and **PpSs+PsPs** arrival times corresponding to crustal thickness h and **Vp/Vs** ratio. The w_i are weighting factors so that $\sum w = 1$. Furthermore the extra condition is set as : $w_1 > w_2 + w_3$ because the slopes of crustal multiples are very similar (Fig. 3.14).

When all phases are stacked coherently then the $s(h, \mathbf{Vp/Vs})$ reaches a maximum which indicates the correct h (crustal thickness) and **Vp/Vs** ratio (Fig. 3.15).
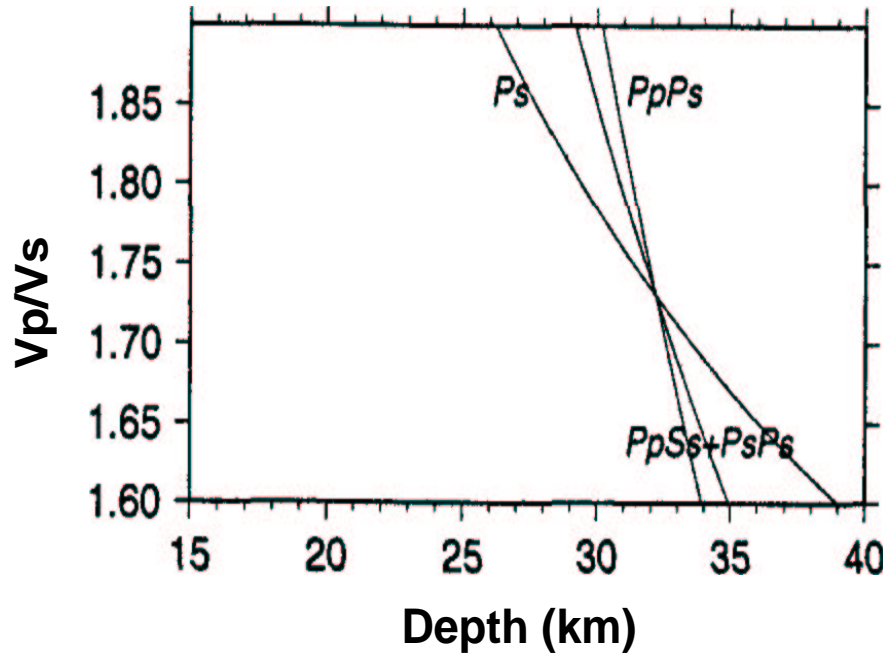

Fig. 3.14 Curves showing the contributions of Ps and its two major crustal multiples to the stacked amplitude $s(h, \mathbf{Vp/Vs})$ as functions of crustal thickness (depth to the Moho) and Vp/Vs. The curves of multiples exhibit similar slopes.

Where receiver functions contain clear Moho conversions and Moho crustal multiples and spread over broad epicentral distances this is method is able to detect the crustal depth as well as average Vp/Vs ratio with rather high precision (Fig. 3.15).

By combining such point data over a seismic network it is possible to produce maps of crustal thickness and Vp/Vs ratios which are indispensable for structural studies.
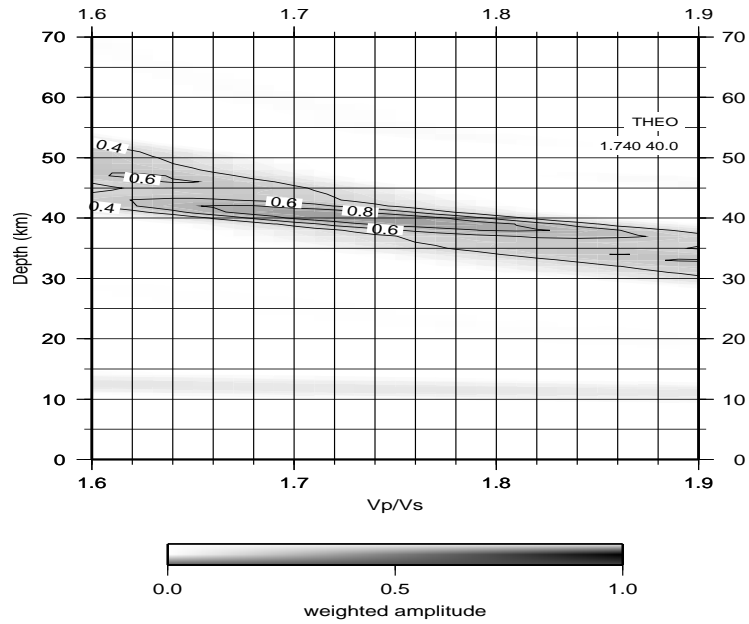
Fig. 3.15 An ideal example of application of the *Zhu & Kanamori (2000)* method to synthetic receiver functions of Fig. 3. 10. The crustal thickness of 40 km and Vp/Vs ratio of 1.74 are among those values used in producing synthetic receiver functions of Fig. 3.10 and have been successfully estimated by this method.